Nonlinear vorticity balance of the Subantarctic Front in the southeast Pacific

T. K. Chereskin,[1] L. D. Talley,[1] and B. M. Sloyan[2,3]

[1] Direct velocity observations from shipboard and lowered acoustic Doppler current profilers are used to examine the velocity and vorticity structure of the Subantarctic Front (SAF) between the East Pacific Rise and Drake Passage from surveys made in 2005 and 2006. The SAF is characterized by meanders of horizontal wavelength approximately 250–300 km in this region of relatively smooth topography. The depth-averaged SAF jet is observed to be closely aligned with the flow at 150 m, as in an equivalent barotropic flow. The barotropic or depth-averaged vorticity exhibits a balance between advection of planetary vorticity and relative vorticity, as would be seen in a Doppler-shifted short barotropic Rossby wave in a mean flow. The implied wave speed is consistent with the observed range of current speeds. An exponential fit to the vertical structure of the current consistent with the vorticity balance suggests a vertical decay scale of about 1900 m. The vorticity balance at 150 m implies a surface divergence which must be balanced at depth by a divergence of the opposite sign. The calculation confirms the tentative conclusions of Hughes (2005) for this region, which were based on a surface climatology but indicates a larger vertical decay scale and wave speed.

1. Introduction

[2] The Southern Ocean is unique in that it is the only ocean that circles the globe without being blocked by land. Its main current, the Antarctic Circumpolar Current (ACC), is a zonally connected conduit for exchange between the major oceans. The reentrant geometry of the Southern Ocean restricts net meridional geostrophic flow to depths below the shallowest topography. High mesoscale variability within the ACC is a key factor in relaxing this constraint, allowing ageostrophic meridional flow via eddies.

[3] The circulation in the ACC region is forced by circumpolar eastward wind stress that, in the vertical integral, is balanced by pressure differences across topography, fluxing angular momentum to the solid Earth via "form stress" [*Munk and Palmén*, 1951]. Transient and standing eddies are thought to be the mechanism by which the eastward momentum is transmitted down through the water column to the level of the topography, and hence, eddies are also central to the zonal momentum balance [*Johnson and Bryden*, 1989; *Hughes and Ash*, 2001; *Olbers et al.*, 2004; *Williams et al.*, 2007].

[1]Scripps Institution of Oceanography, University of California, San Diego, La Jolla, California, USA.
[2]Centre for Australian Weather and Climate Research, CSIRO, Hobart, Australia.
[3]CSIRO Wealth from Oceans National Research Flagship, Hobart, Australia.

[4] Vorticity in the ACC is forced by wind stress curl at the surface and is balanced by pressure differences across topography, which upset the local Sverdrup balance through bottom pressure torques. Numerical modeling results show that bottom pressure torques balance wind stress curl in a zonal integral when averaged over a latitude band in the ACC [*Hughes and de Cuevas*, 2001] but need not balance locally at all longitudes [*Hughes*, 2005]. A number of studies have used potential vorticity conservation as a framework to examine the role of bathymetry in steering the flow [*Gille*, 2003] as well as to determine where vorticity is significantly forced and compensated [e.g., *Hughes*, 2005; *Ochoa and Niiler*, 2007]. Subsurface velocity observations are severely lacking in the Southern Ocean; many studies resolve the flow at a single depth and model the vertical structure as equivalent barotropic (EB), as suggested by numerical models [*Killworth*, 1992; *Killworth and Hughes*, 2002]. In an EB flow, the time-mean velocity is self-similar in the vertical such that the flow at one depth is parallel and proportional to the flow at another depth. The gravest empirical mode technique, which is intrinsically EB, provides observational support by explaining more than 97% of the baroclinic density variance in the ACC [*Sun and Watts*, 2001]. Note that flows that are EB in the time mean are not necessarily so in the time-dependent flow [e.g., *Tracey et al.*, 2006].

[5] The goal of this paper is to diagnose the local dynamics of the ACC from direct velocity observations made in the southeast Pacific between the East Pacific Rise and Drake Passage during 2005 late austral winter and 2006

austral summer. The two surveys comprise 12 crossings of the northernmost front of the ACC, the Subantarctic Front (SAF). Satellite altimetry indicates that sea surface height anomalies were quasi-stationary over the duration (~1 month) of each of the two surveys, which will each be treated as synoptic. The full-depth velocity structure is well resolved from shipboard and lowered acoustic Doppler current profiler (ADCP) observations; in particular, the depth-averaged flow (hereafter referred to as the barotropic flow) can be determined with high accuracy. *Hughes* [2005], using surface measurements and an assumption of EB flow, made predictions about the depth-integrated and depth-dependent ACC vorticity balance. Over complex topography such as in Drake Passage, he predicted a balance between planetary vorticity advection and bottom torque, while over smooth topography (such as our study region), the predicted balance was between planetary and relative vorticity advection, as in a standing barotropic Rossby wave. Our goal is to test the predictions of *Hughes* [2005] in a smooth topography region using subsurface observations that resolve the vertical structure. Objective mapping of the velocity observations consistent with geostrophy is used to produce gridded fields for estimating the nonlinear vorticity balance. We confirm that the barotropic flow in the SAF parallels the direction of the surface jet, which supports an EB interpretation in this region. We find, as *Hughes* [2005] predicted, a balance between the depth-averaged advection of planetary and relative vorticity, with phase speeds consistent with a standing EB Rossby wave. Near the surface we find that relative vorticity advection dominates planetary advection, resulting in a surface divergence which must be balanced at depth by a divergence of the opposite sign.

2. Background

[6] The ACC is supercritical with respect to baroclinic Rossby waves, and unlike lower latitudes where transients propagate to the west, eastward propagation dominates in sea surface height anomalies measured by satellite altimetry [*Hughes et al.*, 1998]. A current that is much faster than the local baroclinic Rossby wave speed can be approximated by an EB structure [e.g., *Killworth and Hughes*, 2002; *Hughes*, 2005]. Potential vorticity conservation in an EB framework requires the current to follow contours of f/h_0, where f is the Coriolis parameter and h_0 is the full-depth integral of a vertical structure function fitted to the velocity field. In the limit of barotropic flow, $h_0 = H$, the water depth, and in the absence of vorticity forcing, advection of planetary and relative vorticity balance, behaving as a stationary barotropic Rossby wave.

[7] Diagnosing meanders of the ACC in the context of the mean vorticity balance has been useful in identifying where vorticity is significantly forced. The steady quasi-geostrophic vorticity equation,

$$\beta \overline{v} + \overline{\mathbf{u} \cdot \nabla \zeta} = f \overline{w_z}, \qquad (1)$$

states that meridional meanders (advection of planetary vorticity, $\beta \overline{v}$) and advection of relative vorticity ($\overline{\mathbf{u} \cdot \nabla \zeta}$) are balanced by stretching ($f \overline{w_z}$). Here β is the northward derivative of the Coriolis parameter f; $\mathbf{u} = (u, v)$, which is the horizontal velocity; w is the vertical velocity, and $\zeta = v_x - u_y$,

which is the relative vorticity. Overbars denote averaging in time, and subscripts denote derivatives. The depth integral of (1) relates the total vorticity advection to the difference between the vertical velocity due to wind stress curl (Ekman pumping) and bottom torque. *Hughes* [2005] argues that in the ACC, wind stress curl appears to be a minor influence in meander dynamics. Using a recent surface climatology as a proxy for the depth-integrated ACC, he found two modes of flow: meanders in which advection of relative and planetary vorticity balance, as in a stationary EB Rossby wave, and a flow with divergence associated with topographic features that he interprets as a scaled measure of bottom torque. Form drag by bottom relief is predicted to be large in Drake Passage but relatively small over the much smoother bathymetry upstream of Drake Passage surveyed by these observations.

3. Observations

[8] The observations consist of conductivity-temperature-depth (CTD), lowered acoustic Doppler current profiler (LADCP), and shipboard acoustic Doppler current profiler (SADCP) measurements from surveys made during 2005 austral winter (AAIW05) and 2006 austral summer (AAIW06) in the high-latitude southeast Pacific (Figure 1). A total of 135 LADCP-CTD stations were occupied in 2005 (21 August to 6 October), and 105 LADCP-CTD stations were occupied in 2006 (30 January to 14 March) by the R/V *Knorr* at a nominal spacing of 55 km. The two surveys occupied the same track in the same order, with only slight deviations, the most significant being greater loss of stations because of weather in 2006. Each survey completed six SAF crossings occupied during the first 4 weeks of the 6 week long cruises. Bathymetry [*Smith and Sandwell*, 1997] varies by less than 500 m along the path of the SAF in this region (Figure 1). Maps of weekly sea surface height (SSH) anomalies were produced by Ssalto/Duacs and distributed by Aviso with support from the Centre National d'Etudes Spatiales (CNES) (http://www.aviso.oceanobs.com/data/). Weekly SSH anomalies during the 2005 survey (Figure 2) suggest there is substantial persistence in the spatial pattern of the height anomalies over the duration of the cruise. A similar pattern of persistence was observed during the 2006 survey (not shown). This suggests that treating the observations from each cruise as synoptic in the analysis is a reasonable approximation. The SSH anomalies will be used to estimate the error in this approximation (i.e., the neglect of ζ_t) for the 150 m vorticity budget.

[9] Wind stress and wind stress curl for the survey periods were examined using spatially blended winds that combine high-resolution satellite data (Quickscat scatterometer) and global weather center reanalyses (National Center for Environmental Prediction (NCEP)) to produce a high temporal and spatial resolution (6 hourly and 0.5 × 0.5 degree) data set [*Chin et al.*, 1998]. The data are available from the Research Data Archive, which is maintained by the Computational and Information Systems Laboratory at the National Center for Atmospheric Research (http://dss.ucar.edu, data set ds744.4).

3.1. LADCP-CTD

[10] The LADCP provides a full-depth profile of ocean current from a self-contained ADCP mounted on the CTD
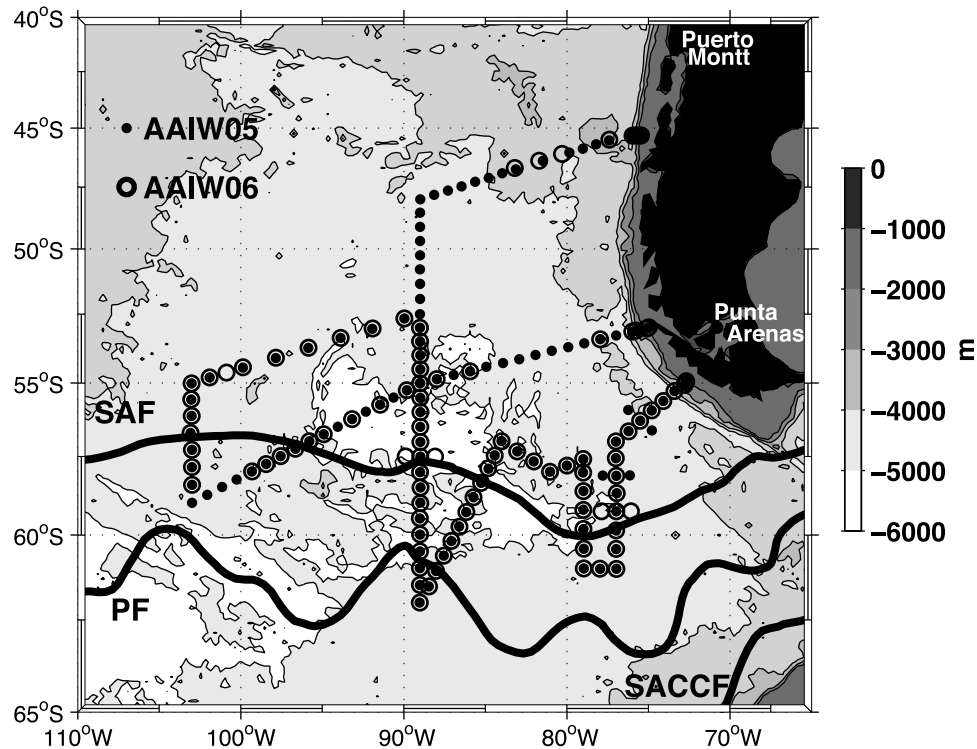
Figure 1. LADCP-CTD station locations and ship track for the austral winter (solid circles, AAIW05) and summer (open circles, AAIW06) surveys. Bathymetry is shown in gray scale with contours every 1000 m. The mean locations of the Subantarctic Front (SAF), Polar Front (PF), and Southern ACC Front (SACCF) from *Orsi et al.* [1995] are denoted by black lines.

rosette. The LADCP was a 4 beam, 153.6 kHz broadband ADCP manufactured by RD Instruments. It had 30° beam angles and was configured to sample in a staggered ping cycle of (1 s, 1.6 s). Other relevant setup parameters were a 16 m vertical bin, pulse, and "blank before transmit." The

data were corrected for the local magnetic declination using model output from the National Oceanographic Data Center Geophysical Data Center. The CTD time series was used to determine velocity scale factor (speed of sound at the
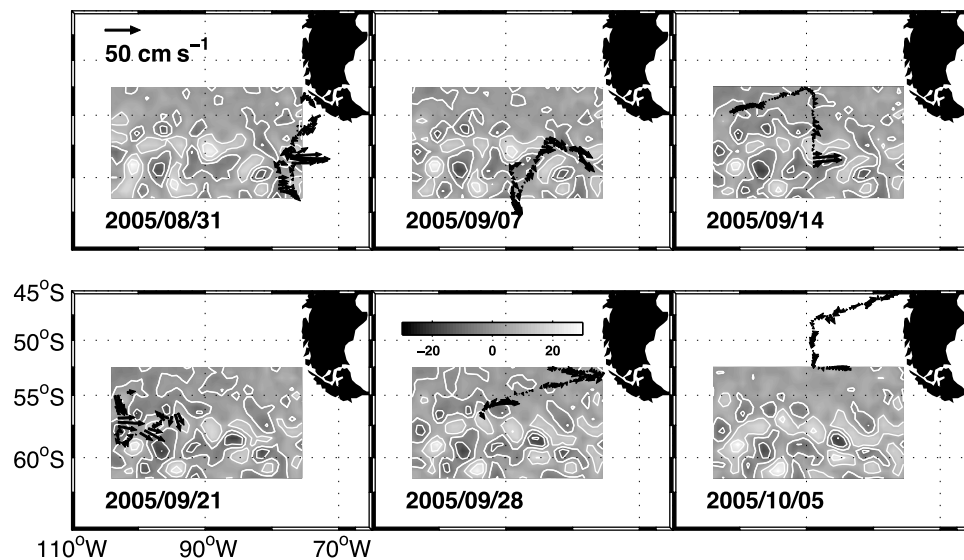

Figure 2. Weekly maps of SSH anomalies from Aviso during the 2005 austral winter survey. The contour interval is 10 cm, and the gray scale (height in centimeters) is shown in the bottom middle frame. Velocity vectors at 150 m depth from the SADCP for the corresponding week of the cruise are superposed. A velocity scale vector is shown in the top left frame.

transducer) and depth. Generally, casts were made to within 10 m of the bottom.

[11] A primary source of error is any time gap in the LADCP profile, causing an uncertain velocity offset (several centimeters per second) between the parts of the profile on either side of the gap. Previous ping interference (ppi), which results from the previous ping reflecting off the bottom and interfering with the current ping, affects velocities in a small (100 m thick) layer about 750 m above bottom (for a sound speed of 1500 m s^{-1}), causing a data gap in the LADCP profile. Pinging asynchronously, as done here, results in two layers, each with reduced sampling from editing out ppi, but avoids complete data loss in either interference layer. A second problem with data loss arises at the bottom of a LADCP-CTD cast, when the package is held 10 m above the seabed, since the blank after transmit exceeds this distance. The stop at the bottom of the cast was minimized (no soaking for the bottom bottle sample) to keep this gap to a minimum.

[12] The processing is the traditional shear method described by *Fischer and Visbeck* [1993] and implemented by Eric Firing in the University of Hawai'i Common Ocean Data Access System (CODAS) LADCP software. Briefly, overlapping profiles of vertical shear of horizontal velocity are averaged and gridded (5 m bins) to form a full-depth shear profile. The shear profile is integrated vertically to obtain the baroclinic velocity, and the resulting unknown integration constant is the depth-averaged or barotropic velocity. This barotropic component is then computed as the sum of the time-averaged, measured velocity and the ship drift (minus a small correction, less than 1 cm s^{-1}, to account for a nonconstant fall rate) [*Fischer and Visbeck*, 1993; *Firing*, 1998]. Errors in the baroclinic profile accumulate as $1/\sqrt{N}$ where N is the number of samples [*Firing and Gordon*, 1990]. The shear standard deviation in these measurements is about 2.5×10^{-3} s^{-1}. The minimum number of measurements per bin is about 100 in the low scattering regime near the bottom, and the maximum is about 600 above the thermocline. This yields a shear standard error about a factor of 10 smaller than the standard deviation. Integrating over 4500 m (nine hundred 5 m segments) results in a velocity error of about 4 cm s^{-1} in the baroclinic profile. The barotropic component is inherently more accurate, because the errors result from navigational inaccuracies alone. These are quite small, about 1 cm s^{-1}, with the military (P code) accuracy GPS available on the *Knorr* (single position fix accuracy of 1 m). Comparisons with Pegasus suggest that the LADCP can measure the depth-averaged velocity to within 1 cm s^{-1} [*Hacker et al.*, 1996]. Because of its higher accuracy and better representativeness (since it is integrated over the 4 h duration of the cast), the barotropic velocity estimated from the LADCP is used in this calculation.

3.2. SADCP

[13] The SADCP data are from a 76.8 kHz Ocean Surveyor phased array ADCP (OS75) manufactured by RD Instruments. The transducer was mounted in an instrument well that was open to the sea and was located at approximately 5 m depth, with beam 3 oriented 45° to starboard. The ADCP was configured to ping in narrowband mode with a 16 m pulse, bin, and "blank before transmit." Single ping ADCP data and ancillary navigation streams from GPS, gyrocompass, and Position and Orientation System for Marine Vessels (POS MV) were collected and processed using University of Hawaii Data Acquisition System (UHDAS) data acquisition and CODAS processing software, written by Eric Firing and Jules Hummon, University of Hawaii. The ADCP measures the velocity relative to the ship. Absolute ocean currents are calculated by removing the ship motion over the ground using the navigation measurements. Gyrocompass was the heading source in real time, and heading corrections were made in postprocessing using the POS MV measurements and an estimated 0.17° transducer misalignment.

[14] Overall, the quality of the navigation data acquired during both surveys was excellent. The estimated accuracy of the POS MV heading corrections is 0.1°, and most importantly, the heading correction procedure removes heading bias. The overall error in ocean currents is estimated at 1–2 cm s^{-1} [*Chereskin and Harris*, 1997]. The main data problems were loss of data from bubble sweepdown (noise) when the bow thruster was used to maintain station and during rough weather and heavy seas. The maximum profiling range of the OS75 was about 850 m, but this depth range was drastically curtailed when bubbles were severe.

4. Objective Mapping

[15] For this study, objective maps of ocean currents subject to a geostrophic constraint are made at two levels from the direct velocity observations: 150 m (SADCP) and depth-averaged or barotropic (LADCP). Errors in the maps can be attributed to several sources: instrument error, ageostrophic currents (tides or inertial), and temporal variability. Instrument error, as discussed in the previous section, is about 1 cm s^{-1}. The barotropic tide predicted by the TPXO6.2 model [*Egbert et al.*, 1994] for the region is of order 1 cm s^{-1} and has been estimated and subtracted from the velocity observations. Long-term SADCP observations in Drake Passage [*Lenn et al.*, 2007] show that inertial currents do not significantly penetrate below the winter mixed-layer depth there (about 120 m), and geostrophic shear is small in the mixed layer [*Lenn and Chereskin*, 2009]. The main objective of these surveys upstream of Drake Passage was to observe formation of Antarctic Intermediate Water (AAIW) during winter, when deep mixed layers form in the high-latitude southeast Pacific, and the subsequent restratification during the following summer [*Talley et al.*, 2006; *Sloyan et al.*, 2009]. Within the AAIW study region, winter mixed layers were almost everywhere deeper than 100 m. The SAF was a sharp southern boundary for the region of deepest mixed layers whose depths exceeded 300 m (Figure 3). During the summer survey, mixed layer depths were everywhere less than 100 m. We consider the currents at 150 m as reasonable estimates of surface geostrophic currents with the caveat that inertial noise is likely larger during the winter survey when this depth lies within the mixed layer, whereas summer survey currents are primarily geostrophic at 150 m. For brevity, the maps using the SADCP 150 m velocity will be referred to as surface maps, and those using the LADCP depth-averaged velocity will be referred to as barotropic. Since the vertical scale of near-inertial motions is small relative to the ocean
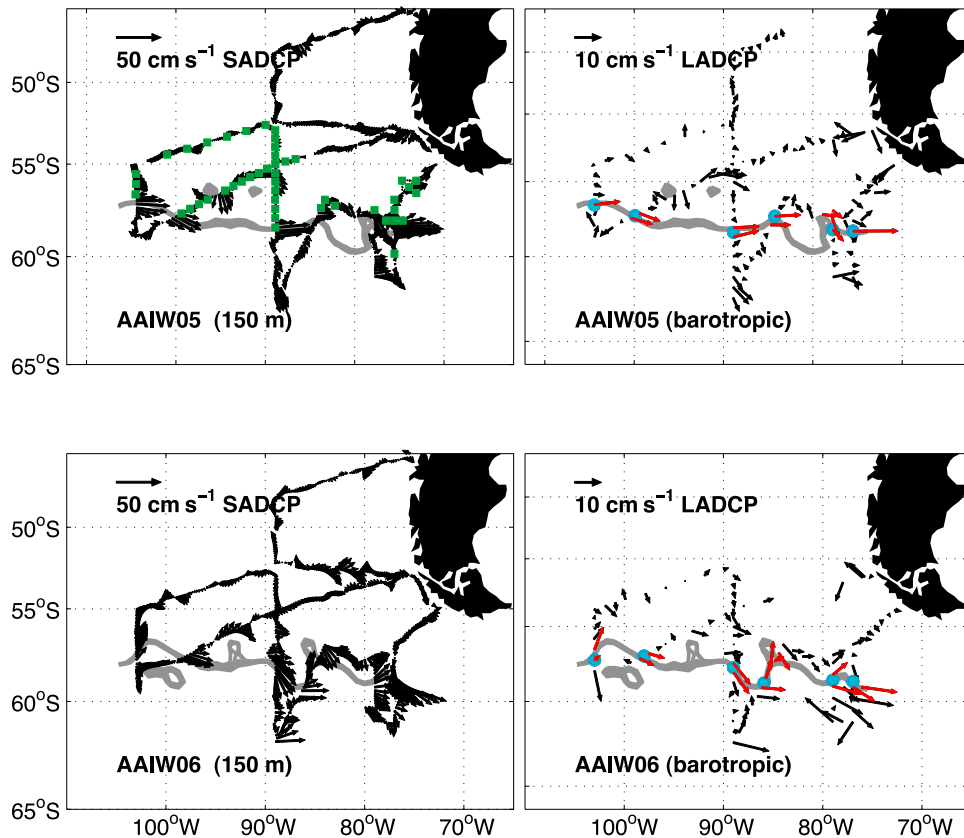
Figure 3. Mapped velocities during the two surveys shown at the original data locations along the track. The gray line is an estimate of the synoptic SAF streamline following *Lenn et al.* [2008]. The SAF locations determined from the CTD data are denoted by the blue filled circles on the LADCP (barotropic) plots. Locations of winter mixed layers deeper than 300 m calculated using the algorithm of *Holte and Talley* [2009] were provided by J. Holte (personal communication, 2009) and are shown as green squares on the AAIW05 150 m plot. No mixed layers deeper than 100 m were observed during AAIW06. The vectors shown in red are used to estimate the mean barotropic velocity of the SAF core (see section 6).

depth, they will contribute negligibly to the barotropic flow. Temporal variability in treating the observations as synoptic is likely the largest additional source of error. This variability might be expected to covary with the signal, i.e., larger variability where the current is largest, and noise in the objective mapping was set to 10% of the signal variance. Mapping to a stream function reduces noise by smoothing as well as enforcing geostrophy.

[16] In order to estimate the terms on the left-hand side of (1), the 150 m and depth-averaged velocity from each survey were objectively mapped using an isotropic Gaussian covariance with a decorrelation scale of 120 km. The form and scale of the covariance are based on observations in Drake Passage, although the scale is chosen to be larger than the 75 km used by *Lenn et al.* [2008] to reflect the broader scale of the ACC jets upstream of the passage. Observations were mapped to a 0.75° longitude × 0.5° latitude grid, or about 50 km horizontal resolution. (Sensitivity to the mapping parameters is discussed in section 5.) An a priori mean was subtracted from the observations. For the surface level, the mean was derived from the dynamic topography of *Maximenko and Niiler* [2005, hereafter MN05]. For the barotropic flow, the mean was derived from the intermediate-depth pressure determined by *Davis* [2005, hereafter Davis] from float data. The velocity residuals and an associated height field (stream function ψ) were mapped such that the geostrophic continuity relation,

$$\nabla \cdot f\overline{\mathbf{U}} = 0, \qquad (2)$$

was satisfied [*Bretherton et al.*, 1976].

[17] The a priori means were added back to the mapped velocities and stream function. The mean fields also satisfy (2). Error maps (in percent) are shown in Figure 4. Fractional error less than 0.5 (50% of the variance explained) corresponds to the lighter gray scale and forms a swath that follows the ship track. Although the horizontal coverage from the SADCP is better than the LADCP, mapping skill is similar except when LADCP stations were dropped because of weather, apparent on the northernmost east-west transect east of 90°W. Maps for 2006 are similar (not shown). The SAF crossings, in particular, have good coverage.

5. Sensitivity to Mapping Parameters and a Priori Means

[18] Estimating the terms of the vorticity budget (1) depends on taking derivatives of the stream function produced by the
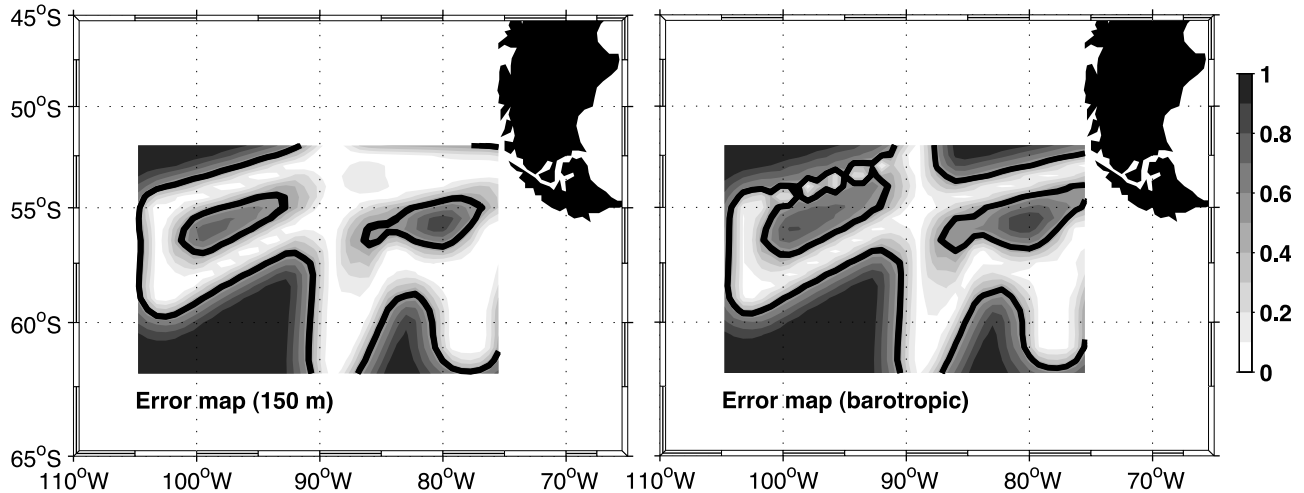
Figure 4. Mapping error for (left) the SADCP data at 150 m and (right) the LADCP barotropic velocity from the 2005 survey. The gray scale for both maps is shown at the far right. The thick line contour is the 0.5 error value and corresponds to 50% skill in the mapping (i.e., mapping accounts for half the signal variance).

objective mapping. Velocity gradients (vorticity) and vorticity gradients must be estimated perpendicular to the track. In this study, derivatives were calculated as centered differences (first differences at the grid boundaries). For the results to be robust, they should not depend critically on the choice of mapping parameters or the a priori means. In this section, the sensitivity of the results to the final choice of mapping parameters (120 km decorrelation scale, 10% noise, and $0.75° \times 0.5°$ grid) and to the a priori means is examined. One surface case (Table 1) and one barotropic case (Table 2) are analyzed in detail.

[19] The climatologies used for the a priori means, MN05 (Figure 5a) and Davis (not shown), are quite smooth. Aviso SSH anomalies from the cruise time period (Figure 2) can be added to the MN05 climatology to produce an a priori mean for the surface stream function (MN05 plus Aviso, Figure 5b) that is more representative of the actual time of the observations. We first address the question, does a more realistic prior improve the stream function significantly (case F, Table 1)?

[20] In objective mapping, the mean is subtracted from the observations, the velocity residuals are mapped, and then the mean is added back. Figure 5 shows the middle step, the mapped residuals (Figures 5d and 5e), for two different priors (Figures 5a and 5b), respectively. These can be viewed as the corrections made by the SADCP observations to the mean. When the data are of good quality and coverage, the mapping should be relatively insensitive to the mean, and one goal is to use the sensitivity to the prior to define the limit of high-quality coverage. The mapped residuals using the MN05 prior (Figure 5d) are much larger than those using the MN05 plus Aviso prior (Figure 5e), indicating that the SADCP data make a much bigger correction to the smooth climatology. The final objective analysis (OA) map, with the MN05 mean added back in, is shown in Figure 7a. Differences from the final OA map using the MN05 plus Aviso prior are small (Figure 5f) and occur at the edges of the study region where, in the absence of SADCP data, the OA mapped solution relaxes to the mean. The difference thus highlights the region outside the influence of the data as determined by the decorrelation scale. Within a decorrelation scale of the track, differences in the mean used in mapping the SADCP data have little effect. In addition to using a more realistic a priori surface

Table 1. Sensitivity to Mapping Parameters for AAIW05 150 m Case[a]

Case	Prior	L (km)	dx (°E)	dy (°N)	e	uRMS (cm s^{-1})	vRMS (cm s^{-1})	Correlation	b	Degrees of Freedom
A	MN05	120	0.75	0.50	0.10	6.2	6.3	−0.60 (0.07)	−2.0 (0.3)	296
B	MN05	120	0.75	0.50	0.05	5.9	6.1	−0.42 (0.09)	−1.7 (0.4)	316
C	MN05	120	0.75	0.50	0.20	6.5	6.4	−0.68 (0.06)	−2.1 (0.3)	278
D	MN05	80	0.75	0.50	0.10	5.0	5.3	−0.51 (0.10)	−2.4 (0.6)	184
E	MN05	150	0.75	0.50	0.10	6.9	6.5	−0.65 (0.05)	−1.9 (0.2)	383
F	MN05A	120	0.75	0.50	0.10	6.1	6.1	−0.55 (0.08)	−2.3 (0.4)	296
G	Davis	120	0.75	0.50	0.10	6.1	6.0	−0.51 (0.08)	−1.6 (0.3)	291
H	MN05	120	0.50	0.25	0.10	6.2	6.3	−0.54 (0.04)	−2.9 (0.3)	900
I	MN05	120	1.00	0.75	0.10	6.2	6.3	−0.44 (0.13)	−1.2 (0.4)	124

[a]A priori means were MN05 [*Maximenko and Niiler*, 2005], MN05 plus Aviso anomalies averaged over the cruise time period (MN05A), and Davis [*Davis*, 2005]. Mapping decorrelation scale (L), grid spacing (dx, dy), and error parameter (e) were varied. The root-mean-square differences (uRMS and vRMS) between the observed and mapped velocities, the correlation, and the regression (b) coefficients between the nonlinear ($\mathbf{u} \cdot \nabla \zeta$) and planetary ($\beta v$) advection terms are estimated for each case. Ninety-five percent confidence limits based on the Student t test are given in parentheses. Correlation and regression are calculated over the map domain where the fractional error is less than 0.2; the degrees of freedom are based on the number of samples used.

Table 2. Sensitivity to Mapping Parameters for AAIW05 Barotropic Case[a]

Case	Prior	L (km)	dx (°E)	dy (°N)	e	uRMS (cm s^{-1})	vRMS (cm s^{-1})	Correlation	b	Degrees of Freedom
A	Davis	120	0.75	0.50	0.10	1.9	1.5	−0.79 (0.05)	−1.0 (0.1)	188
B	Davis	120	0.75	0.50	0.05	1.6	1.3	−0.72 (0.06)	−0.9 (0.1)	218
C	Davis	120	0.75	0.50	0.20	2.3	1.7	−0.82 (0.05)	−1.1 (0.1)	149
D	Davis	80	0.75	0.50	0.10	1.3	1.0	−0.78 (0.07)	−1.5 (0.2)	100
E	Davis	150	0.75	0.50	0.10	2.3	1.7	−0.81 (0.04)	−0.8 (0.1)	264
F	MN05	120	0.75	0.50	0.10	2.6	1.9	−0.74 (0.06)	−1.4 (0.2)	190
G	Davis	120	0.50	0.25	0.10	1.9	1.5	−0.71 (0.04)	−1.3 (0.1)	569
H	Davis	120	1.00	0.75	0.10	1.9	1.5	−0.76 (0.08)	−0.7 (0.1)	90

[a]A priori means were Davis [*Davis*, 2005] and MN05 [*Maximenko and Niiler*, 2005]. Mapping decorrelation scale (L), grid spacing (dx, dy), and error parameter (e) were varied. The root-mean-square differences (uRMS and vRMS) between the observed and mapped velocities, the correlation, and the regression (b) coefficients between the nonlinear ($\mathbf{u} \cdot \nabla \zeta$) and planetary ($\beta v$) advection terms are estimated for each case. Ninety-five percent confidence limits based on the student t test are given in parentheses. Correlation and regression are calculated over the map domain where the fractional error is less than 0.2; the degrees of freedom are based on the number of samples used.

mean, a less realistic smoother mean (Davis) was used (case G, Table 1). In all three cases (A, F, and G), the RMS difference between the observations and the mapped currents at the original data locations are small (about 6 cm s^{-1}).

[21] Improving the prior estimate does not improve the SADCP stream function within a decorrelation scale of the track. Examining the sensitivity to the prior is useful, however, in determining the map cutoff for the estimate of the nonlinear term. We find that the vorticity gradients are insensitive to the a priori mean within the 0.2 fractional error contour (80% variance explained) marked on Figure 5f, and the statistics (correlation and regression) agree within 95% confidence (cases A, F, and G in Table 1). In this analysis, we will display stream function out to 0.8 and maps of derived quantities out to 0.6 fractional error in order to emphasize patterns. Generally, some proxy for the ship track will be present, and it should be remembered that the highest skill lies within 100 km of the track. The vorticity budget statistics (correlation and regression), however, are calculated using estimates that fall within the 0.2 fractional error contour so that the mean has negligible influence on the statistics.

[22] Since the Aviso product (Figure 5c) provides an alternate source of observations, at least for the surface, one can also ask whether it provides a better source than the SADCP data. The main tradeoff is resolution versus coverage. The SSH anomalies have coverage over the entire mapping grid but are themselves a smoothed and mapped product. *Ducet et al.* [2000] describe the production of the Aviso maps. The SSH anomalies are first low-pass filtered with a 70 km cutoff wavelength and then merged by objective mapping assuming a spatial decorrelation length scale of about 100 km at the latitude of Drake Passage. *Lenn et al.* [2007] show that geostrophic velocity anomalies calculated from Aviso contain significantly less total variance than SADCP anomalies at all wavelengths in Drake Passage. They find that the Aviso anomalies account for 56% of the SADCP variance at wavelengths greater than 100 km but only 3% at wavelengths less than 100 km. This underestimate of the variability in our study region can be seen by the size of the correction that the SADCP observations make to the MN05 plus Aviso (Figure 5e). While smaller than the correction to MN05, it is significant; most importantly, the SAF is narrower and sharper in the SADCP observations, corresponding to a larger gradient and larger currents than estimated from Aviso.

[23] Sensitivity to the other mapping parameters was also examined, varying the error parameter by a factor of 2 and the grid spacing and the decorrelation scale by 50%. The RMS of the fit is improved slightly when the error parameter is decreased (case B, Table 1) and when the decorrelation scale is decreased (case D, Table 1). Both of these cases require a tighter fit to the data, and, in case D, a decrease in the degrees of freedom resulting in larger error bars. A coarser grid (case I, Table 1) also results in larger confidence limits from the decrease in degrees of freedom. A similar variation of parameters for one barotropic case is shown in Table 2, and a variation in prior using the MN05 climatology (case F, Table 2).

[24] While the maps are not sensitive to the smoothness of the priors within the data region, they are greatly improved by a prior that has a background gradient, i.e., the presence of a SAF. Specifying a constant or zero mean produces a nonrealistic map. We conclude that the maps do not depend critically on the choice of mapping parameters and a priori means within reasonable variations. The sensitivity study also provides an estimate of the range of uncertainty in the statistics (correlation and regression columns of Tables 1 and 2).

6. Mean Flow

[25] The depth-averaged and 150 m mapped velocities for the two surveys are shown in Figure 3. In each case, the mapped estimates are shown at the original data locations, and the RMS differences between observed and mapped velocities for the final mapping parameter choices are given in Table 3. Consistent with the expected errors, the residual for the 150 m maps is about 6 cm s^{-1}, small compared to the jet amplitude of 40 cm s^{-1}. The residual for the barotropic maps is about 1 cm s^{-1}, small compared to peak barotropic jet amplitudes of 10 cm s^{-1}.

[26] Stream function height values for the SAF were determined following *Lenn et al.* [2008]. The gray lines in Figure 3 mark the location of the SAF streamlines in the 150 m stream function maps (full stream functions are shown in Figures 7a and 8a). The surface SAF contours are also shown on the respective barotropic maps in Figure 3 to provide a visual correlation between 150 m and barotropic velocities along the SAF path. The SAF streamlines have good correspondence with the locations of mapped velocity jets, also showing some strong meanders and detached
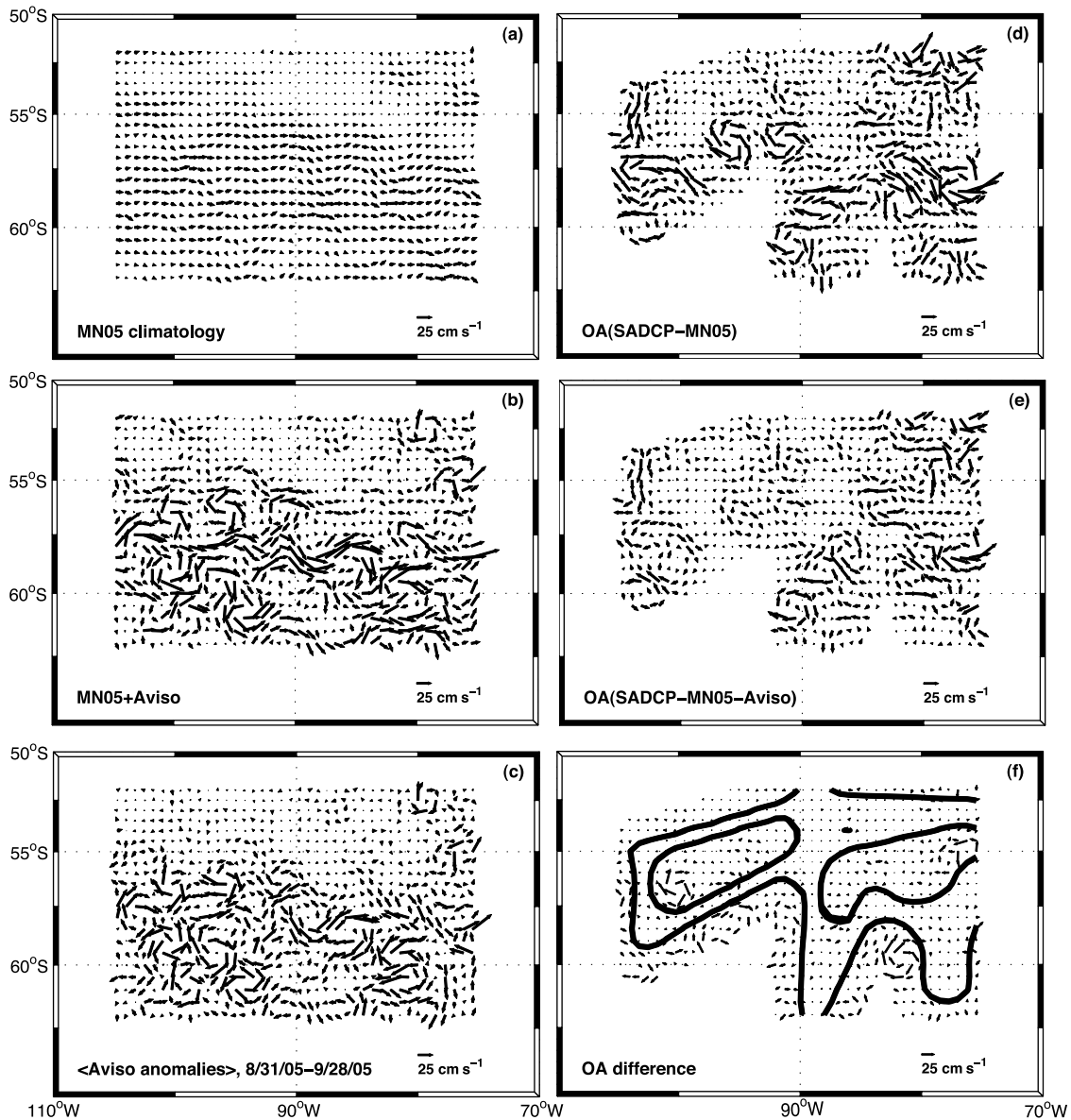
Figure 5. Sensitivity of the AAIW05 150 m map to two different a priori means: the *Maximenko and Niiler* [2005] climatology (MN05) and the climatology added to the mean Aviso anomalies (MN05 plus Aviso) from 31 August 2005 to 28 September 2005 shown in Figure 2. Geostrophic velocity calculated from (a) MN05, (b) MN05 plus Aviso, and (c) the Aviso anomalies alone are shown. The objective analysis of the observed velocity residuals (SADCP minus the mean) for (d) the MN05 prior and (e) the MN05 plus Aviso prior are shown to the right of their respective means (Figures 5a and 5b). The final OA map with the MN05 prior is shown in Figure 7a. (f) The final OA map with the MN05 plus Aviso prior is very similar; only the difference between the two OAs is shown. The thick contour indicates 80% variance explained (less than 0.2 fractional error).

eddies along the path of the SAF. In particular, for AAIW05, a pair of eddies can be seen north of the main SAF front, between 100°W and 90°W, in both the velocities and the closed streamlines. For AAIW06, a pair of meanders with very strong curvature can be seen along the SAF path. Using the CTD observations to locate the density front of the SAF (blue dots, Figure 3) confirms the streamline analysis.

[27] The range of barotropic speeds estimated in the core of the SAF from geostrophically mapped LADCP observations is 3–16 cm s^{-1} (red vectors, Figure 3). The time-mean barotropic velocity in the core is $(6.6 \pm 0.7, 0.7 \pm 0.9)$ cm s^{-1}. In the SAF latitude range, 55°S–60°S, the angle between the mapped velocity at 150 m and the mapped barotropic velocity was examined. Approximately 74% (92%) of the angles in the 2005 (2006) surveys were 5° or less, suggesting that the 150 m and barotropic flow along the path of the SAF were parallel in this region.

[28] The strong vertical coherence of the velocity suggested fitting a vertical structure function to the LADCP

Table 3. Mapping Error, Correlation, and Regression[a]

Cruise	Depth	uRMS (cm s^{-1})	vRMS (cm s^{-1})	Correlation	b	Degrees of Freedom
AAIW05	150	6.2	6.3	−0.60 (0.07)	−2.0 (0.3)	296
AAIW06	150	4.2	4.5	−0.65 (0.06)	−3.0 (0.4)	307
AAIW05[b]	150	6.2	6.3	−0.50 (0.08)	−1.1 (0.2)	296
AAIW06[b]	150	4.2	4.5	−0.65 (0.06)	−1.9 (0.2)	307
AAIW05	barotropic	1.9	1.5	−0.79 (0.05)	−1.0 (0.1)	188
AAIW06	barotropic	1.4	1.1	−0.60 (0.09)	−1.1 (0.2)	161

[a]A priori means were MN05 [*Maximenko and Niiler*, 2005] for 150 m and Davis [*Davis*, 2005] for the barotropic cases, respectively. Decorrelation scale (120 km), grid spacing (0.75°E, 0.5°N), and error parameter ($e = 0.1$) were the same for all cases. The root-mean-square difference (uRMS and vRMS) between the observed and mapped velocities, the correlation, and the regression (b) coefficients between the nonlinear ($\mathbf{u} \cdot \nabla\zeta$) and planetary ($\beta v$) advection terms are estimated for each case. Ninety-five percent confidence limits based on the student t test are given in parentheses. Correlation and regression are calculated over the map domain where the fractional error is less than 0.2; the degrees of freedom are based on the number of samples used.
[b]Correlation and regression coefficients estimated between ($\mathbf{u} \cdot \nabla\zeta$) and ($\zeta_t + \beta v$).

observations. Velocity profiles in Drake Passage are consistent with an exponential vertical decay (Y. L. Firing et al., manuscript in preparation, 2010). If an exponential $A(z) = \exp(z/L)$ is assumed for the AAIW region, then the decay scale L can be estimated from a regression of the depth-weighted barotropic current $u^{baro}H$ versus the 150 m velocity u^{surf} (Figure 6). We found L in the AAIW region to range from 1150 to 1900 m using LADCP profiles in water of depth exceeding 2500 m (eliminating coastal profiles). The mean depth of the ocean for the profiles used in the fit was 4600 m.

7. Vorticity Balance

7.1. Surface (150 m) Balance

[29] Mapped velocity and velocity stream function, ψ, at 150 m during the 2005 survey are shown in Figure 7a. The relative vorticity of this flow field is small (not shown); the peak values are found in the SAF jets and are of order 10% of local f, indicating quasi-geostrophy is an appropriate assumption. The two advection terms on the left-hand side of (1) are shown in Figures 7b and 7c. The advection of planetary vorticity (Figure 7c), while small, is a first-order quantity in the sense that v is O(10) cm s^{-1} and β, while small, can be computed precisely. The sign of this term is determined by v, and the meandering SAF gives rise to alternating bands of positive and negative planetary vorticity advection. Nonlinear advection of relative vorticity (Figure 7b) is anticorrelated with and generally larger than planetary advection (Table 3). The nonlinear advection term (Figure 7b) also displays bands of alternating sign; these bands are reduced but not canceled by the opposite-signed advection of planetary vorticity within meridional meanders (Figure 7d). The contribution of ζ_t is shown in Figure 7e, estimated from the change in the SSH anomalies over a 5 week interval. This contribution is of the same order as the planetary advection term, but it is not significantly correlated with either advection term. Adding ζ_t to the planetary advection reduces the correlation with the nonlinear term from −0.6 to −0.5 and also reduces the linear regression from −2.0 to −1.1
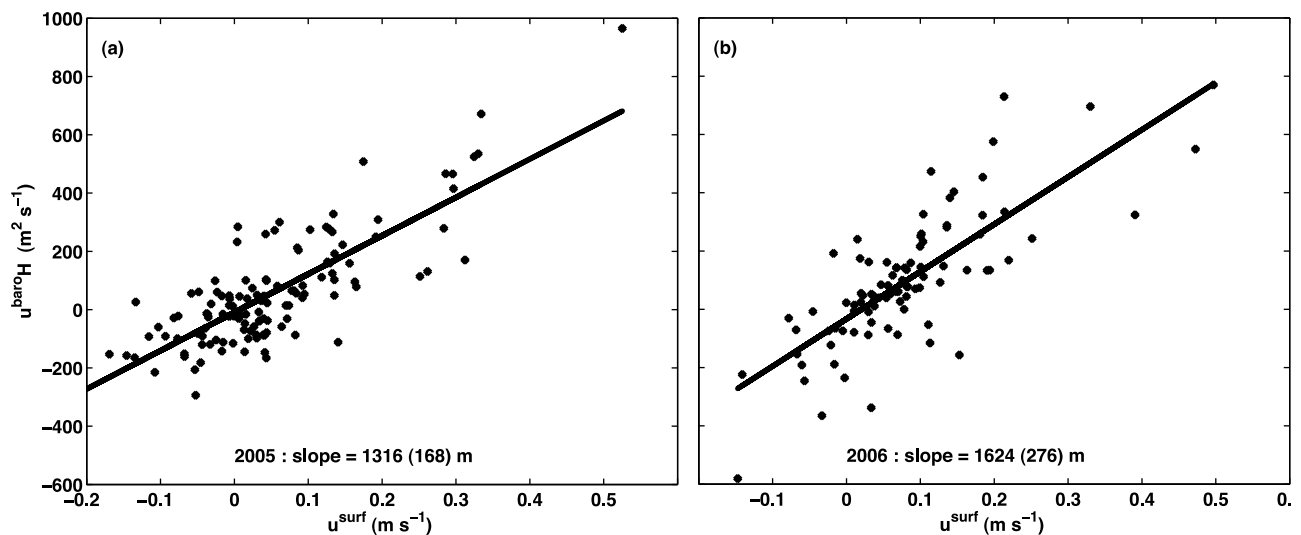

Figure 6. Regression of the depth-integrated current ($u^{baro}H$) versus the surface current (u^{surf}) using LADCP data from (a) AAIW05 and (b) AAIW06. Only the eastward component was used in the fit. The slope provides an estimate of the vertical decay scale of an exponential vertical structure function. Uncertainty in the slope is given in parentheses. LADCP observations used in the fit were in water of depth $H > 2500$ m. The "surface" current estimate is averaged over the duration of the LADCP cast (typically about 4 h) and over the upper 150 m in order to reduce high-frequency noise.
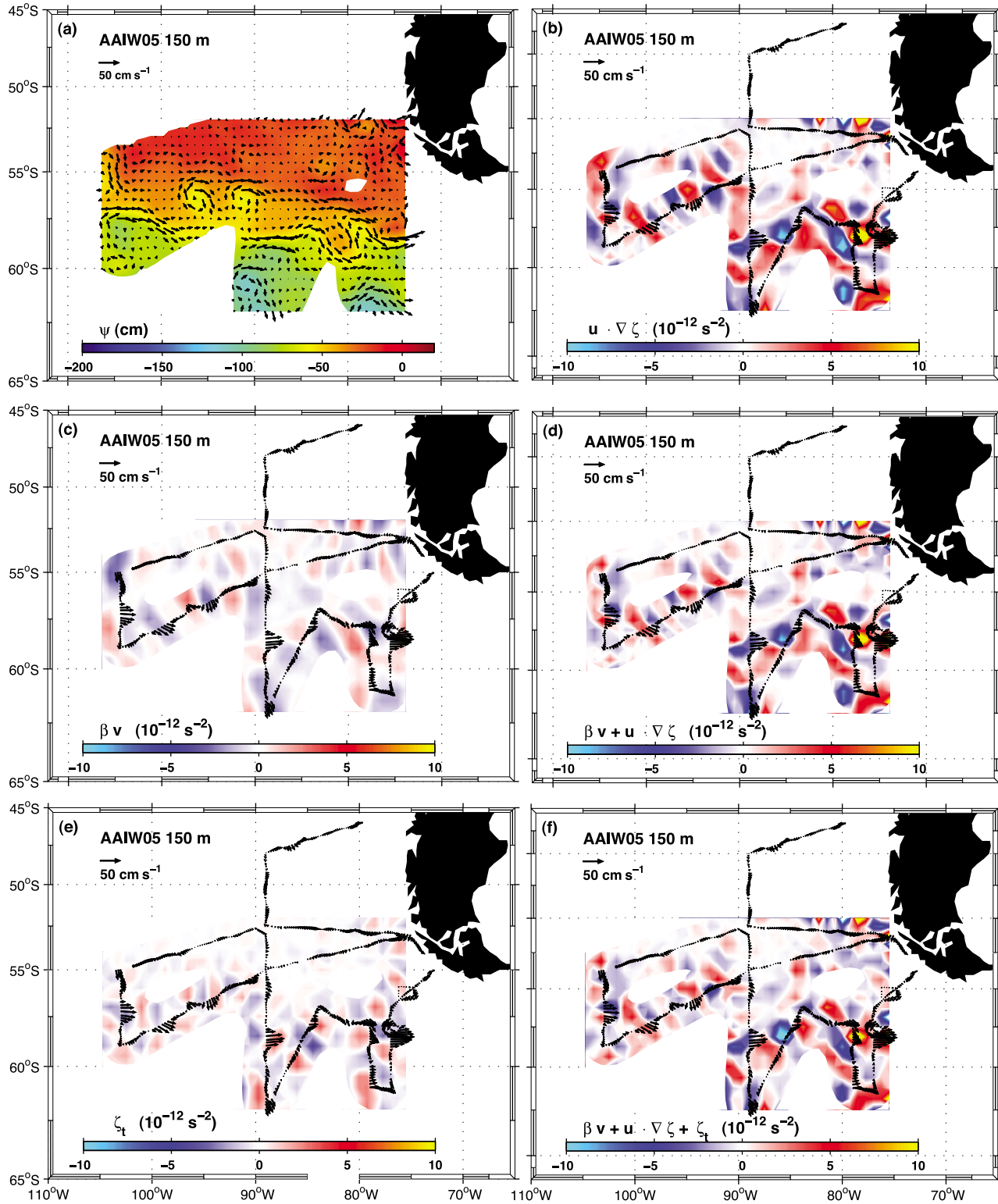
Figure 7. Velocity and vorticity budget at 150 m during AAIW05: (a) mapped velocity and stream function, (b) relative vorticity advection, (c) planetary vorticity advection, (d) total advection based on summing Figures 7b and 7c, (e) time derivative of relative vorticity estimated from Aviso SSH anomalies, and (f) the vorticity budget based on summing Figures 7b, 7c, and 7e. The mapped currents at the original data locations are shown in Figures 7b–7f to indicate the ship track and the SAF jet location.

(Table 3). The vorticity budget including the time-dependent term is still dominated by the nonlinear advection term (Figure 7f).

[30] Results for the vorticity budget (1) estimated from the second survey (Figure 8) are very similar. As before, the size of the ζ_t term (Figure 8e) is of the same order as the βv term (Figure 8c). For this survey, however, the time-dependent term is negatively correlated with the planetary advection (−0.4) and positively correlated with the nonlinear advection (0.3). Adding ζ_t to the planetary advection does not change its correlation with the nonlinear term (−0.65) but reduces the regression from −3.0 to −1.9 (Table 3). The vorticity budget including the time-dependent term is still dominated by the nonlinear advection term (Figure 8f).

7.2. Barotropic (Depth-Averaged) Balance

[31] A map of the depth-averaged velocity and stream function, ψ, during the 2005 survey is shown in Figure 9a. As at 150 m depth, the relative vorticity is small (not shown); the peak values are again found in the SAF jets and are of order 3%–5% of local f. The two advection terms on the left-hand side of (1) are shown in Figures 9b and 9c, respectively. Advection of planetary and nonlinear advection of relative vorticity are nonzero only in the southern part of the survey region, along the path of the SAF. They are anticorrelated and generally about the same size. The magnitudes are small, but the signs appear robust, with bands of alternating sign in the individual advection terms that cancel. The correlation between the two advection terms calculated over the domain of the map with errors less than 0.2 for the 2005 survey is −0.79. Maps for the 2006 survey (Figure 10) show similar patterns and a correlation of −0.60. The regression is about −1 in each case, and Table 3 gives the 95% confidence limits on these statistics.

8. Discussion

[32] Because the Rossby number of the flow is small ($\zeta/f < 0.1$), the assumption of quasi-geostrophy is appropriate, and we have used geostrophic currents estimated from the mapped stream functions to make the next order correction in the vorticity budget, the nonlinear advection term in (1). We find, as did *Hughes* [2005], that nonlinear advection is significant along the path of the SAF and acts to compensate the advection of planetary vorticity. The two fields appear as bands of alternating sign, with a zonal length scale of about 250–300 km and an elongated meridional scale of about 500 km. Qualitatively, the balance of terms at the surface indicates a divergence whereas the terms approximately balance using the barotropic current. Sections 8.1–8.4 attempt to quantify these results.

8.1. Surface Balance

[33] One of *Hughes* [2005] predictions, based on an assumed EB vertical structure, is that the vorticity balance of the ACC in the region considered here, between the East Pacific Rise and Drake Passage, is that of a quasi-stationary EB Rossby wave, with a depth-mean balance between advection of planetary and relative vorticity. Assuming quasi-geostrophy and an EB structure for both the mean flow and the meanders, *Hughes* [2005] reformulated the depth-integrated vorticity balance in terms of the surface

current, ($u^{\text{surf}}, v^{\text{surf}}$). Keeping the same notation, we assume the currents are given by the geostrophic relation, $u = -g\eta_y/f$, $v = g\eta_x/f$, where g is gravity, and the sea surface height displacement η (related to the pressure anomaly, p', where $p' = \rho_0 g\eta$) is given by

$$\eta = A(z)\left[\frac{-u^{\text{surf}}fy}{g} + C\ \exp\ (ikx)\right], \qquad (3)$$

where $A(z)$ is the vertical structure function, z is positive upward, $A(0) = 1$, and k is the horizontal wave number of the meanders. In the depth integral, the stretching term on the right hand side of (1) equates to the difference between surface wind stress curl and bottom torque. Over the relatively flat topography of the region, it is reasonable to expect that the bottom torque is small.

[34] Integrating (1) from the seafloor $z = -H$ to the sea surface $z = 0$ and assuming $w(-H) = 0$ yields

$$h_0\beta v^{\text{surf}} + h_1 u^{\text{surf}} v^{\text{surf}}_{xx} = \frac{\nabla \times \tau}{\rho_0}, \qquad (4)$$

where $h_0 = \int_{-H}^{0} A(z)\mathrm{d}z$, $h_1 = \int_{-H}^{0} A^2(z)\mathrm{d}z$, τ is the wind stress, and ρ_0 is the density of seawater. *Hughes* [2005] points out that the EB assumption implies a divergence at the surface, even over a flat bottom, because the vertical decay scale of the two advection terms differs: βv is proportional to $A(z)$ whereas $\mathbf{u} \cdot \nabla \zeta$ is proportional to A^2. The ratio of these terms is negative because of being anticorrelated and proportional to h_0/h_1, which for $A(z) = \exp(z/L)$ is 2. This is a good match to the estimated regression coefficients for these terms which range from −1.1 to −3 (Table 3). An estimate of the surface wind stress curl divided by density, averaged over the primary month of each cruise, is shown in Figure 11. The pattern of wind stress curl does not show the banded structure seen in the vorticity advection terms. The contribution of the forcing term relative to advection in (4) is estimated as $(\nabla \times \tau)/h_0\rho_0$, and for h_0 of $O(10^3)$ m, it is $O(10^{-13})$ s^{-2}, an order of magnitude smaller than estimates of the advection terms.

8.2. Barotropic Balance

[35] We can make an analogous formulation for the depth-averaged vorticity budget using the barotropic velocities, ($u^{\text{baro}}, v^{\text{baro}}$). Integrating (1) from the seafloor $z = -H$ to the sea surface $z = 0$ and averaging over the depth H yields

$$\beta v^{\text{baro}} + H h_1/(h_0)^2 u^{\text{baro}} v^{\text{baro}}_{xx} = \frac{\nabla \times \tau}{H\rho_0}. \qquad (5)$$

The depth-averaged balance has only the barotropic velocity in the linear term. The nonlinear term requires weighting by the factor $H h_1/(h_0)^2$, which for $A(z) = \exp(z/L)$ is $H/2L$. Using the estimates of $L = (1150, 1900)$ from section 6 and $H = 4600$ m, this weighting factor ranges from 2 to 1.2. As calculated here, the expected regression coefficient for the advective terms estimated using the barotropic velocity is negative (because they are anticorrelated) and is the inverse of the weighting factor. The estimated regression coefficients range from −1.5 to −0.7 (Table 2) and are in reasonable agreement with the range from −0.8 to −0.5 estimated from
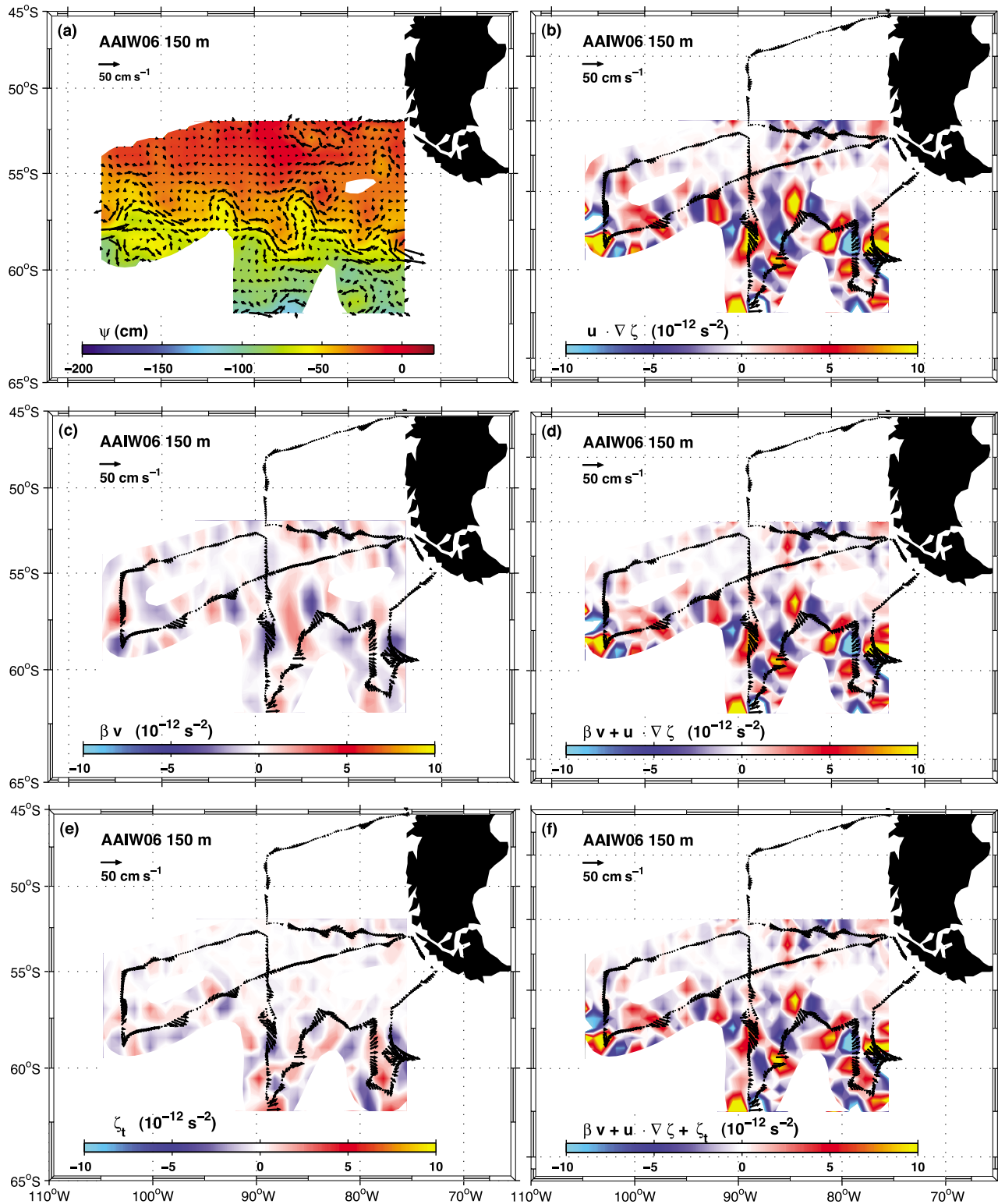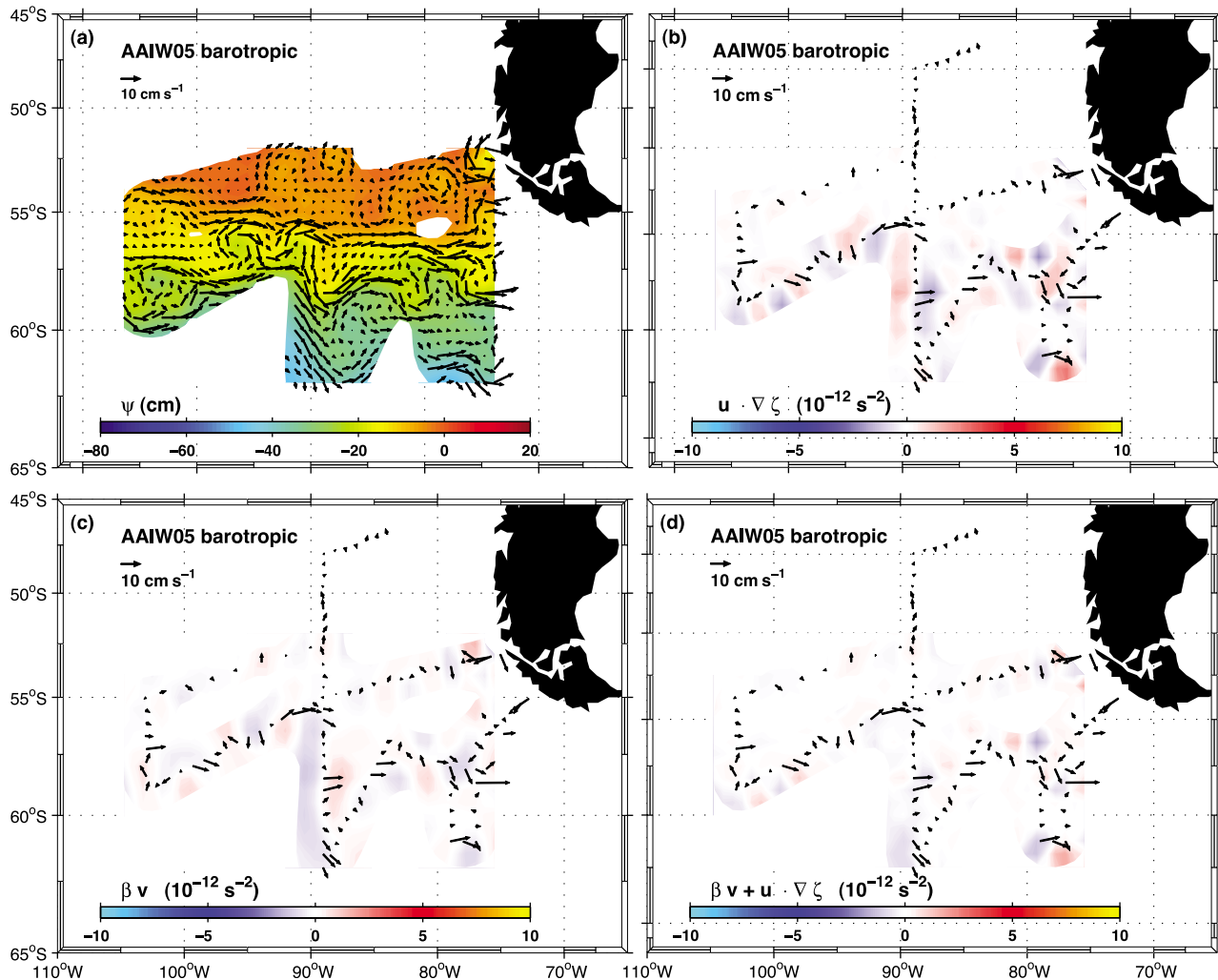
Figure 8. Velocity and vorticity budget at 150 m during AAIW06: (a) mapped velocity and stream function, (b) relative vorticity advection, (c) planetary vorticity advection, (d) total advection based on summing Figures 8b and 8c, (e) time derivative of relative vorticity estimated from Aviso SSH anomalies, and (f) the vorticity budget based on summing Figures 8b, 8c, and 8e. The mapped currents at the original data locations are shown in Figures 8b–8f to indicate the ship track and the SAF jet location.

Figure 9. Depth-averaged velocity and vorticity budget during AAIW05: (a) mapped velocity and stream function, (b) relative vorticity advection, (c) planetary vorticity advection, (d) total advection based on summing Figures 9b and 9c. The mapped currents at the original data locations are shown in Figures 9b–9d to indicate the ship track and the SAF jet location.

$-2L/H$. The contribution of the forcing term relative to advection in (5) is estimated as $(\nabla \times \tau)/H\rho_0$, and for H of $O(10^3)$ m, it is $O(10^{-13}\ \text{s}^{-2})$, an order of magnitude smaller than estimates of the advection terms.

[36] The improved balance of the vorticity budget using the barotropic velocity estimates is somewhat serendipitous; it is due to the appropriate weighting factor being closer to unity, which depends in turn on the vertical structure of the flow. Thus, the regression coefficients determined for both the surface and barotropic balance are consistent with an exponential EB structure, and finding regression coefficients close to -1 for the barotropic component implies that the longer vertical decay scale (1900 m) is a better fit to the observed vorticity budget. Using the high-end estimate suggests a vertical decay scale that is significantly longer than the h_0 of about 1400 m that *Hughes* [2005] estimates using a vertical structure function fit to the Ocean Circulation and Climate Advanced Modeling (OCCAM) model

[*Killworth and Hughes*, 2002]. The higher estimate suggested here is consistent with fitted exponential decay scales in the range 1500–2000 m for the SAF in Drake Passage (Firing et al., manuscript in preparation, 2010).

[37] In principle, the EB structure predicts a divergence of the opposite sign at depth. Although we tried to further examine the depth-dependent balance, the problem that we encountered was poor signal-to-noise in the deep LADCP currents. The LADCP observations lack the good horizontal resolution of the SADCP, and unlike the barotropic component, which is the most robust current component that can be calculated, the expected "signal" of the deep sub-thermocline currents of the ACC is of the same order as the noise (temporal variability), and error dominates the maps of velocity at deep levels.

8.3. Dispersion Relation

[38] Substituting for v^{surf} in (4) using the geostrophic relation and (3) and assuming free waves (i.e., neglecting the
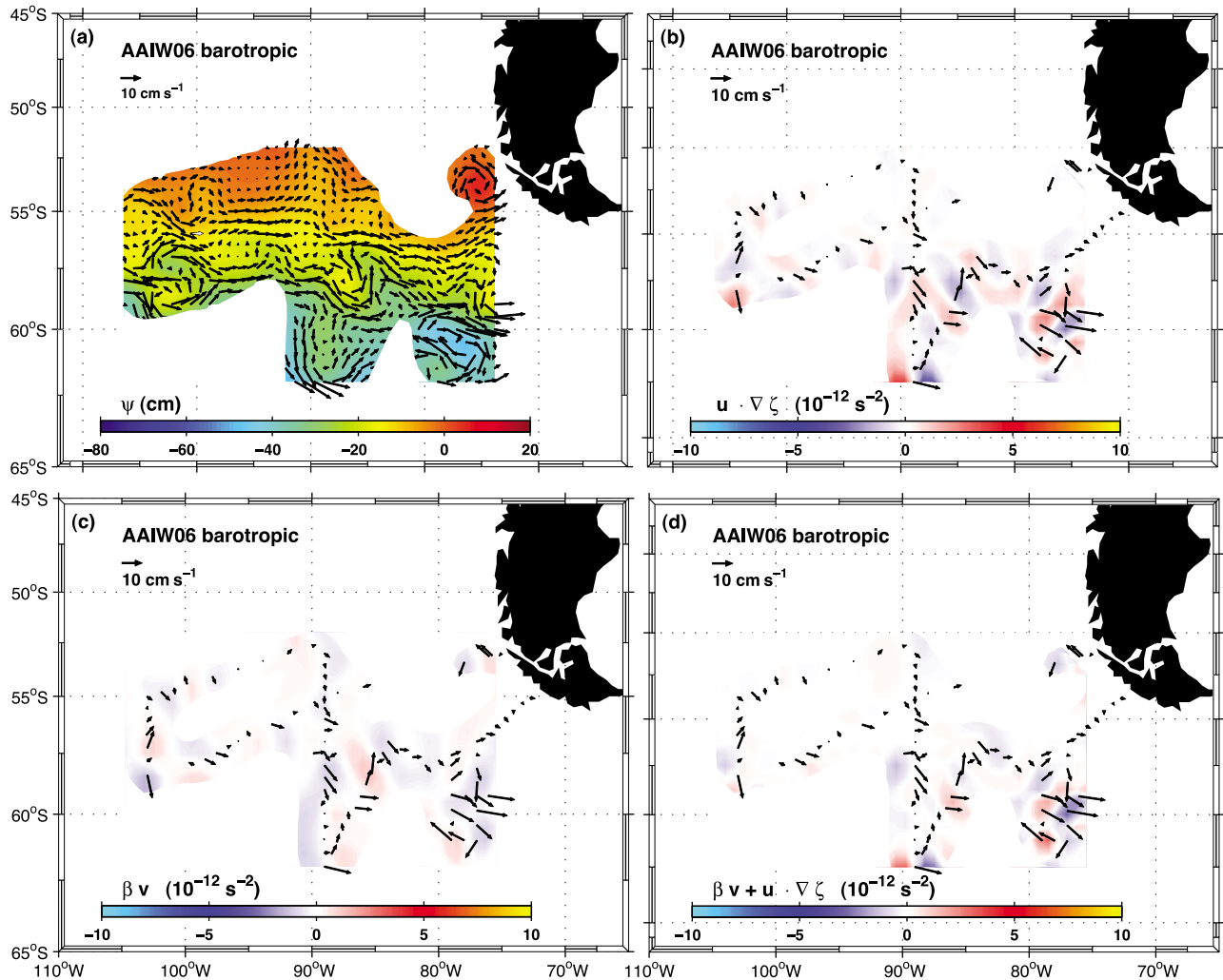
Figure 10. Depth-averaged velocity and vorticity budget during AAIW06: (a) mapped velocity and stream function, (b) relative vorticity advection, (c) planetary vorticity advection, (d) total advection based on summing Figures 10b and 10c. The mapped currents at the original data locations are shown in Figures 10b–10d to indicate the ship track and the SAF jet location.

wind forcing) yields a prediction of the phase speed of stationary waves in terms of the surface current,

$$u^{\text{surf}} = \frac{\beta}{k^2} \left(\frac{h_0}{h_1} \right). \qquad (6)$$

Using a value of $\beta = 1.3 \times 10^{-11} \text{ m}^{-1} \text{ s}^{-1}$ appropriate for 56°S and a ratio $h_0/h_1 = 2$ based on an exponential vertical structure, then for a zonal wavelength of 500 km, the phase speed for a stationary EB meander is 16 cm s^{-1}. A wavelength of 300 km, which is a better match to these observations, would correspond to a phase speed of 6 cm s^{-1}, much smaller than the observed surface speeds in the SAF. The meridional velocity curvature, $-u_{yy}$, however, is larger than the planetary gradient, β. For these observations, the effective β, given by $\beta_{\text{eff}} = \beta - u_{yy}$ is about a factor of five larger than planetary β in the core of the SAF jet, with a correspondingly larger phase speed estimated from (6), about 30 cm s^{-1} for a meander wavelength of 300 km and a good match for the observed surface currents.

8.4. Time Dependence

[39] The quasi-stationary wave interpretation appears consistent with the range of observed speeds and with the sea surface height anomalies that appear to propagate more slowly than the surface current (Figure 2). The evaluation of the time-dependent term for the surface balance, however, suggests that this term is of the same order as planetary advection, though much smaller than nonlinear advection. Time dependence in the surface layer was found to be correlated with both advection terms during the summer but not during the winter survey, suggesting that the quasi-steady assumption is a better fit to the winter observations. Alternatively, additional inertial noise in the advective terms estimated for the winter survey might explain the decrease in correlation with the time-dependent term, which is purely geostrophic since it is calculated from SSH anomalies. This seems unlikely, however, since it did not have any apparent decrease on the correlation between the advection terms, which are about as well correlated as in summer. One
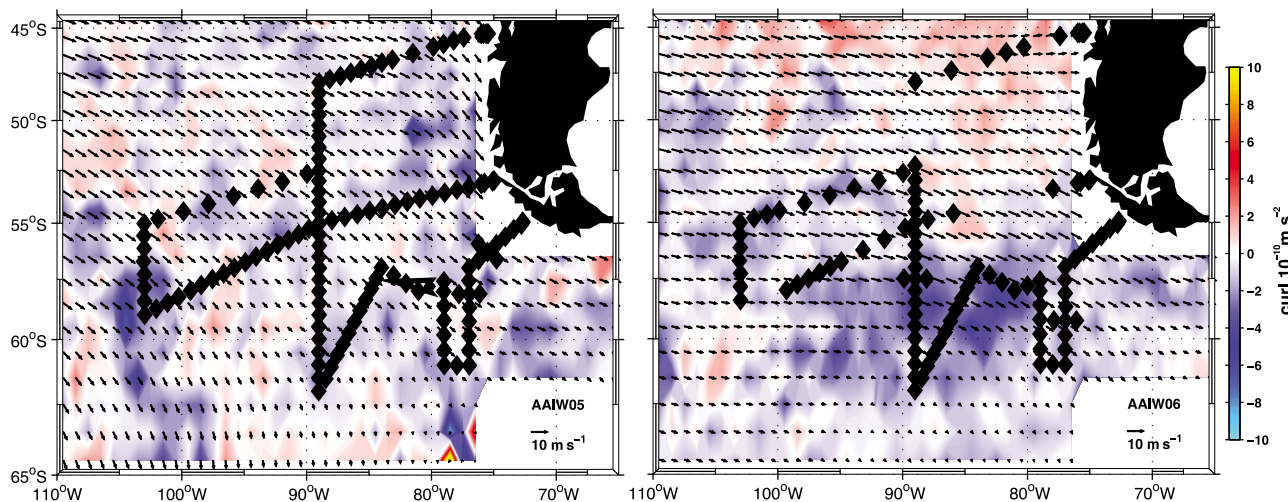
Figure 11. Quickscat-NCEP blended wind: monthly mean wind velocity on the mean wind stress curl divided by density, $(\nabla \times \tau)/\rho_0$, where $\rho_0 = 1025$ kg m^{-3}. (left) Monthly mean for AAIW05 was calculated for September 2005. (right) Monthly mean for AAIW06 was calculated for February 2006. A scale velocity vector is shown in the bottom right of each plot. The color bar units are 10^{-10} m s^{-2}. Black diamonds mark locations of LADCP-CTD stations.

consequence of the presence of a quasi-stationary front during winter is that the deep mixed layers (300–500 m deep) observed immediately north of the SAF (Figure 3) maintain position relative to the front during the seasonal ventilation of AAIW and its precursor in the mixed layer, Subantarctic Mode Water. Numerical modeling of the mixed layer formation and its relation to the front is a topic of further investigation.

9. Conclusions

[40] The regional dynamics of the SAF in the southeast Pacific were diagnosed through its velocity and vorticity structure. Direct velocity observations made during surveys in 2005 and 2006 provide an accurate estimate of the depth-averaged flow from LADCP observations and of the flow at 150 m from SADCP observations. The direct velocity observations improve on the resolution of the SAF over the Aviso-mapped SSH anomalies.

[41] The depth-averaged SAF jet was observed to be closely aligned with the jet at 150 m, as in an EB flow. The time-mean zonal surface current in the SAF jet is about 40 cm s^{-1}, while the depth-averaged current is about 7 cm s^{-1}. The SAF is characterized by meanders with zonal wavelength of about 250–300 km in which depth-averaged advection of planetary and relative vorticity balance to leading order, as in a quasi-stationary EB Rossby wave. The observed balance is consistent with an exponential EB structure with a vertical decay scale close to 1900 m, and the range of current speeds are consistent with estimates of EB wave phase speeds. This balance was first suggested by *Hughes* [2005] using a surface climatology and a vertical structure function from the OCCAM model, but it remained to be confirmed by subsurface observations. The vertical decay scale and phase speed determined from these observations are larger than those estimated by *Hughes* [2005].

[42] The vorticity balance at 150 m depth in the meanders reveals a residual divergence that is dominated by the nonlinear advection of relative vorticity. Poor signal-to-noise ratio in the deep currents precludes estimating the balance at depth, but the depth-averaged result suggests that the dominance should reverse at depth. The interpretation of quasi-stationary meanders is consistent with the observation that transients in the ACC propagate more slowly to the east than the surface current.

References

Bretherton, F. P., R. E. Davis, and C. B. Fandry (1976), A technique for objective analysis and design of oceanographic experiments applied to MODE-73, *Deep Sea Res. Oceanogr. Abstr.*, *23*, 559–582.

Chereskin, T. K., and C. L. Harris (1997), Shipboard acoustic Doppler current profiling during the WOCE Indian Ocean Expedition: I10, *Tech. Rep. SIO 97-14*, Scripps Inst. of Oceanogr., Univ. of Calif., San Diego, La Jolla.

Chin, T. M., R. F. Milliff, and W. G. Large (1998), Basin-scale, high-wavenumber sea surface wind fields from a multiresolution analysis of scatterometer data, *J. Atmos. Oceanic Technol.*, *15*, 741–763.

Davis, R. E. (2005), Intermediate-depth circulation of the Indian and South Pacific Oceans measured by autonomous floats, *J. Phys. Oceanogr.*, *35*, 683–707.

Ducet, N., P. Y. L. Traon, and G. Reverdin (2000), Global high-resolution mapping of ocean circulation from TOPEX/Poseidon and ERS-1 and -2, *J. Geophys. Res.*, *105*, 19,477–19,498.

Egbert, G. D., A. F. Bennett, and M. G. G. Foreman (1994), TOPEX/ Poseidon tides estimated using a global inverse model, *J. Geophys. Res.*, *99*, 24,821–24,852.

Firing, E. (1998), Lowered ADCP development and use in WOCE, *Int. WOCE Newsl.*, *30*, 10–14. (Erratum, *Int. WOCE Newsl.*, *31*, 20, 1998.)

Firing, E., and R. Gordon (1990), Deep ocean acoustic Doppler current profiling, in *Proceedings of the IEEE Fourth Working Conference on Current Measurement*, pp. 192–201, IEEE Press, New York.

Fischer, J., and M. Visbeck (1993), Deep velocity profiling with self-contained ADCPs, *J. Atmos. Oceanic Technol.*, 10, 764–773.

Gille, S. T. (2003), Float observations of the Southern Ocean. Part 1: Estimating mean fields, bottom velocities, and topographic steering, *J. Phys. Oceanogr.*, 33, 1167–1182.

Hacker, P., E. Firing, W. D. Wilson, and R. Molinari (1996), Direct observations of the current structure east of the Bahamas, *Geophys. Res. Lett.*, 23, 1127–1130.

Holte, J., and L. Talley (2009), A new algorithm for finding mixed layer depths with applications to Argo data and subantarctic mode water formation, *J. Atmos. Oceanic Technol.*, 26, 1920–1939, doi:10.1175/2009JTECHO543.1.

Hughes, C. W. (2005), Nonlinear vorticity balance of the Antarctic Circumpolar Current, *J. Geophys. Res.*, 110, C11008, doi:10.1029/2004JC002753.

Hughes, C. W., and E. R. Ash (2001), Eddy forcing of the mean flow in the Southern Ocean, *J. Geophys. Res.*, 106, 2713–2722.

Hughes, C. W., and B. A. de Cuevas (2001), Why western boundary currents in realistic oceans are inviscid: A link between form stress and bottom pressure torques, *J. Phys. Oceanogr.*, 31, 2871–2885.

Hughes, C. W., M. S. Jones, and S. Carnochan (1998), Use of transient features to identify eastward currents in the southern ocean, *J. Geophys. Res.*, 103, 2929–2944.

Johnson, G. C., and H. L. Bryden (1989), On the size of the Antarctic Circumpolar Current, *Deep Sea Res., Part A*, 36, 39–53.

Killworth, P. D. (1992), An equivalent-barotropic mode in the Fine Resolution Antarctic Model, *J. Phys. Oceanogr.*, 22, 1379–1387.

Killworth, P. D., and C. W. Hughes (2002), The Antarctic Circumpolar Current as a free equivalent-barotropic jet, *J. Mar. Res.*, 60, 19–45.

Lenn, Y.-D., and T. K. Chereskin (2009), Observations of Ekman Currents in the Southern Ocean, *J. Phys. Oceanogr.*, 39, 768–779.

Lenn, Y. D., T. K. Chereskin, J. Sprintall, and E. Firing (2007), Mean jets, mesoscale variability and eddy momentum fluxes in the surface-layer of the Antarctic Circumpolar Current in Drake Passage, *J. Mar. Res.*, 65, 27–58.

Lenn, Y.-D., T. K. Chereskin, and J. Sprintall (2008), Improving estimates of the Antarctic Circumpolar Current streamlines in Drake Passage, *J. Phys. Oceanogr.*, 38, 1000–1010.

Maximenko, N., and P. P. Niiler (2005), Hybrid decade-mean global sea level with mesoscale resolution, in *Recent Advances in Marine Science and Technology*, edited by N. Saxena, pp. 55–59, PACON Int., Honolulu, Hawaii.

Munk, W. H., and E. Palmén (1951), Note on the dynamics of the Antarctic Circumpolar Current, *Tellus*, 3, 53–55.

Ochoa, J., and P. P. Niiler (2007), Vertical vorticity balance in meanders downstream the Agulhas retroflection, *J. Phys. Oceanogr.*, 37, 1740–1744, doi:10.1175/JPO3064.1.

Olbers, D., D. Borowski, C. Völker, and J.-O. Wölff (2004), The dynamical balance, transport and circulation of the Antarctic Circumpolar Current, *Antarct. Sci.*, 16(4), 439–470, doi:10.1017/S0954102004002251.

Orsi, A. H., T. Whitworth III, and W. D. Nowlin Jr. (1995), On the meridional extent and fronts of the Antarctic Cirumpolar Current, *Deep Sea Res., Part I*, 42(5), 641–673.

Sloyan, B. M., L. D. Talley, T. K. Chereskin, R. Fine, and J. Holte (2009), Antarctic Intermediate Water and Subantarctic Mode Water Formation in the southeast Pacific: The role of turbulent mixing, *J. Phys. Oceanogr.*, doi:10.1175/2010JPO4114.1, in press.

Smith, W. H. F., and D. T. Sandwell (1997), Global seafloor topography from satellite altimetry and ship depth soundings, *Science*, 277, 1956–1962.

Sun, C., and D. Watts (2001), A circumpolar gravest empirical mode for the Southern Ocean hydrography, *J. Geophys. Res.*, 106, 2833–2855.

Talley, L. D., T. K. Chereskin, J. Holte, and Y. D. Lenn (2006), Subantarctic Mode Water and Antarctic Intermediate Water formation near the Subantarctic Front in the southeast Pacific in winter 2005, *Eos Trans. AGU*, 87(36), Ocean Sci. Meet. Suppl., Abstract OS32G-01.

Tracey, K. L., D. R. Watts, C. S. Meinen, and D. S. Luther (2006), Synoptic maps of temperature and velocity within the Subantarctic Front south of Australia, *J. Geophys. Res.*, 111, C10016, doi:10.1029/2005JC002905.

Williams, R. G., C. Wilson, and C. W. Hughes (2007), Ocean and atmosphere storm tracks: The role of eddy vorticity forcing, *J. Phys. Oceanogr.*, 37, 2267–2289.

T. K. Chereskin and L. D. Talley, Scripps Institution of Oceanography, University of California, San Diego, La Jolla, CA 92093-0230, USA. (tchereskin@ucsd.edu; ltalley@ucsd.edu)

B. M. Sloyan, Centre for Australian Weather and Climate Research, CSIRO, GPO 1538, Hobart, Tas 7001, Australia. (bernadette.sloyan@csiro.au)